Templated vanadium tellurites: identifying the effects of low density attractions on inorganic layer topology

Xiwen Jia, Jessica L. Dixon, Matthias Zeller,[†] Joshua Schrier[‡] and Alexander J. Norquist[*]

Department of Chemistry, Haverford College, Haverford PA 19041
[†] Department of Chemistry, Purdue University, West Lafayette IN 47907
[‡] Department of Chemistry, Fordham University, Bronx, NY 10458

Abstract

Exploration of the NH_4VO_3 / Na_2TeO_3 / 2,4,6-triaminopyrimidine / H_2O system yielded the formation of two new phases, $[C_4H_8N_5][VO_3]$ and $[C_4H_8N_5]_2[V_2Te_2O_{10}]$. Phase selection in this system is largely dictated by the tellurium concentration during reaction. Differences in the $[V_2Te_2O_{10}]_n^{2n-}$ layer topologies in $[C_4H_8N_5]_2[V_2Te_2O_{10}]$ and two related phases, $[C_6H_{16}N_2][V_2Te_2O_{10}]$ and $[C_5H_{14}N_2][V_2Te_2O_{10}]$ were probed using noncovalent interaction energy ratios. These ratios allow for one to directly visualize and quantify differences in intermolecular interaction strengths between compounds. The presence or absence of π - π stacking interactions between organic ammonium cations in $[C_4H_8N_5]_2[V_2Te_2O_{10}]$ and two related phases, $[C_6H_{16}N_2][V_2Te_2O_{10}]$ and $[C_5H_{14}N_2][V_2Te_2O_{10}]$ are the source of layer connectivity differences. These π - π interactions between 2,4,6-triaminopyrimidinium cations in $[C_4H_8N_5]_2[V_2Te_2O_{10}]$ dictate their orientations between $[V_2Te_2O_{10}]_n^{2n-}$ layers, and direct the locations of hydrogen-bonding interactions. Effects associated with reactant concentrations, charge density matching

---

[*] Author to whom correspondence should be addressed.
Haverford College
370 Lancaster Avenue
Haverford PA, 19041 USA
tel (610) 896 2949
fax (610) 896 4963
email anorquis@haverford.edu
http://www.haverford.edu/chem/Norquist/

and intermolecular interactions were probed using composition space analyses, Iterative Hirshfeld partial atomic charge, molecular surface area calculations and noncovalent interaction index calculations, respectively.

keywords: hydrothermal crystal growth, vanadium tellurite, noncovalent interaction indices, noncovalent interaction energy ratios

Introduction

Organic inorganic hybrid materials constitute an exceptionally diverse class of compounds that have been the focus of intense interest for many decades. Several subclasses have been reported to exhibit interesting physical properties, providing the drive for their extended study. For example, metal organic frameworks have long been studied as storage media,[1-2] metal halide perovskites have attracted considerable attention as photovoltaic devices[3] and organically templated metal oxides can exhibit catalytic activity, act as a molecular sieve and show nonlinear optical activity.[4-5]

Organically templated metal oxides exhibit exceptional compositional and structural diversity. The metal centers that have been included in such materials span the periodic table, resulting in a wide range of compositions and connectivities.[6-9] This behavior effectively precludes both the design of specific three-dimensional structures[10] and the prediction of connectivities from reactant and reaction data.[11-14] As such, the development of new compounds primarily relies upon exploratory syntheses. Strategies for deriving chemical information from exploratory work generally involve two main components, reaction outcome dependence upon either reactant properties[15-22] or reaction conditions.[23-25] Reactant properties can include variables such as chemical hardness,[17] framework acidity[18, 20] and amine structure,[5, 15-16, 26] while reaction conditions are often focused on relative reactant concentrations[24-25] and pH.[23] These strategies generally rely upon the isolation of specific reaction variables, in an attempt to ascribe outcome differences to the variable being studied.

This study is designed to directly probe the effects of both reaction conditions and specific reactant properties on the formation of organically templated vanadates and vanadium tellurites. Exploration of the NH_4VO_3 / Na_2TeO_3 / 2,4,6-triaminopyrimidine / H_2O system resulted in the formation of two new compounds, $[C_4H_8N_5][VO_3]$ and $[C_4H_8N_5]_2[V_2Te_2O_{10}]$. Differences in the crystallization fields for these two compounds are discussed both with respect to one another and in relation to two related systems: $NaVO_3$ / Na_2TeO_3 / 2-methylpiperazine / H_2O and $NaVO_3$ / Na_2TeO_3 / 2,5-dimethylpiperazine / H_2O. The role of charge density matching is investigated, as are the effects of amine structure on vanadium tellurite layer connectivity. Noncovalent interaction index calculations were used to identify, quantify and visualize the cation – cation, anion – anion and cation – anion interactions in $[C_4H_8N_5]_2[V_2Te_2O_{10}]$, $[C_6H_{16}N_2][V_2Te_2O_{10}]$[27] and $[C_5H_{14}N_2][V_2Te_2O_{10}]$.[27] This computation technique allows for one to better understand the structural differences between these three compounds.

1. Experimental

2.1. Materials. NH_4VO_3 (99 %), Na_2TeO_3 (99 %) and 2,4,6-triaminopyrimidine (tapyr, 97 %) were purchased from Sigma-Aldrich. All reagents were used as received. Deionized water was used in these syntheses.

2.2. Syntheses. All reactions were conducted in 23 mL poly(fluoro-ethylene-propylene) lined pressure vessels. Initial reaction pHs were controlled by the addition of 4 M HCl and 4 M NaOH. The reactions were heated to 90 ºC and allowed to soak for 18.5 h. The reactions were then cooled to room temperature at a rate of 6 ºC h^{-1} to promote the growth of large single crystals. Autoclaves and bottles were opened in air, and products were recovered via vacuum filtration.

2.3. $[C_4H_8N_5][VO_3]$ (1) was synthesized as colorless blocks through the reaction of 0.1351 g (1.156×10^{-3} mol) NH_4VO_3, 0.3516 g (2.813×10^{-3} mol) tapyr and 8.9414 g (4.962×10^{-1} mol) H_2O. The initial pH was set to 7. The approximate fill percent of 23 mL reaction vessel was 40 %.

2.4. $[C_4H_8N_5]_2[V_2Te_2O_{10}]$ (2) was synthesized as yellow needles through the reaction of 0.1454 g (1.244×10^{-3} mol) NH_4VO_3, 0.1354 g (6.110×10^{-4} mol) Na_2TeO_3, 0.0858 g (6.864×10^{-4} mol) tapyr and 9.3163 g (5.170×10^{-1} mol) H_2O. The initial pH was set to 7. The approximate fill percent of 23 mL reaction vessel was 45 %.

2.5. Single Crystal X-ray Diffraction.

Data for **1** were collected using a Rigaku Rapid II R-axis curved image plate diffractometer with a Cu-Kα X-ray microsource (λ = 1.54178 Å) with a laterally graded multilayer (Goebel) mirror for monochromatization. A single crystal was mounted on a Mitegen micromesh mount using a trace of mineral oil and cooled *in-situ* to 100(2) K for data collection. Frames were collected using the dtrek option of CrystalClear-SM Expert 2.1 b32,[28] reflections were indexed and processed with HKL3000,[29] and the files scaled and corrected for absorption using Scalepack.[29] Data for **2** were collected using a Bruker AXS Smart Apex CCD with Mo-Kα radiation (λ = 0.71073 Å). The instrument features a fine focus sealed tube X-ray sources with a graphite monochromator. A single crystal was mounted on a Mitegen micromesh mount using a trace of mineral oil and cooled *in-situ* to 100(2) K for data collection. Frames were collected, reflections were indexed and processed, and the files scaled and corrected for absorption using APEX2.[30] For both structures, the heavy atom positions were determined using SIR92.[31] All other non-hydrogen sites were located from Fourier difference maps. All non-hydrogen sites were refined using anisotropic thermal parameters with full matrix least squares procedures on F_o^2 with $I > 3\sigma(I)$. Hydrogen atoms were placed in geometrically idealized positions. All calculations were performed using Crystals *v*. 14.23*c*.[32] Relevant crystallographic data are listed in Table 1.

2.6. Powder X-ray Diffraction. Powder diffraction patterns were recorded on a GBC-Difftech MMA powder diffractometer. Samples were mounted on glass plates. Calculated powder patterns were generated from single crystal data using ATOMS *v.* 6.0.[33] Powder X-ray diffraction patterns were consistent with patterns predicted from the refined single crystal structures of **1** and **2**.

2.7. Infrared Spectroscopy. Infrared measurements were obtained using a Perkin Elmer FT-IR Spectrum 1000 spectrophotometer. Samples were diluted with spectroscopic grade KBr and pressed into pellets. Scans were collected over the range of 400 – 4000 cm^{-1}.

2.8. Bond Valence Sums. Bond valence sums[34] calculations were performed using parameters compiled by Brese and O'Keeffe.[35] Complete tables of bond valence sums for compounds **1, 2**, $[C_6H_{16}N_2][V_2Te_2O_{10}]$ and $[C_5H_{14}N_2][V_2Te_2O_{10}]$ are available in Appendix A.

2.9. Electronic Structure Calculations. Solid-state electronic structure calculations were performed using ABINIT *v*6.4.1.[36-37] ABINIT calculations used the Perdew-Burke-Ernzerhof generalized gradient approximation (PBE-GGA) exchange-correlation functional, norm-conserving Troullier-Martins pseudopotentials, a planewave basis set with energy cutoff of 25 Hartrees, a 6 × 6 × 6 Monkhorst-Pack k-point sampling grid, and experimental crystal structures. Electron localization functions (ELFs) were calculated from the self-consistent valence electron densities and visualized using Vesta *v*3.2.1.[38]

2.10. Surface area calculations. Surface areas for the inorganic components in $[C_4H_8N_5]_2[V_2Te_2O_{10}]$, $[C_6H_{16}N_2][V_2Te_2O_{10}]$ and $[C_5H_{14}N_2][V_2Te_2O_{10}]$ were calculated using a rolling-sphere algorithm by Richards[39] (using the DMS program[40]). Lone pair positions were defined as local maxima in the ELF isosurfaces, with radii of 1.5 Å, based upon Galy's work.[41-42] Calculated surface areas are listed in Table 2.

2.11. Iterative-Hirshfeld charges. Iterative Hirshfeld (Hirshfeld-I)[43-44] atomic partial charge determinations were performed on the self-consistent valence electron density in conjunction with all-electron atomic charge densities generated using the HF96 atomic Hartree-Fock code,[45] as described in our previous work.[5] A table of partial atomic charges for **2** is provided in Appendix A.

2.12. Non-covalent Interaction (NCI) Index Calculations. NCI analyses were performed using CRITIC 2 version 1.0[46-47] to generate promolecular densities from the default numerical free-atom densities, using an approach similar as in a previous report.[19] The extraction of isosurfaces corresponding to particular interactions was performed using Mathematica 10.0.0.0 and visualized using Vesta v.3.3.6.[38] The calculation of interaction energy ratios were performed using numerical integrations, as described both below and in an earlier report.[19]

2. Results and discussion

A composition space diagram[24, 27, 48-52] was constructed from the NH_4VO_3 / Na_2TeO_3 / tapyr / H_2O system by conducting 28 individual reactions. Each reaction contained a combined total of 0.025 moles of reactants (V, Te and tapyr) and approximately 9 g of solvent water. The heating times and cooling rates (18.5 h and -6 ºC h^{-1}), initial reaction pH (7) and container volume (23 mL) were consistent between reactions. The relative V : Te : tapyr mole ratios were systematically varied between individual reactions. Reaction products were identified using powder and single crystal X-ray diffraction and infrared spectroscopy. The identities of the major products for each reaction are plotted in Figure 1.

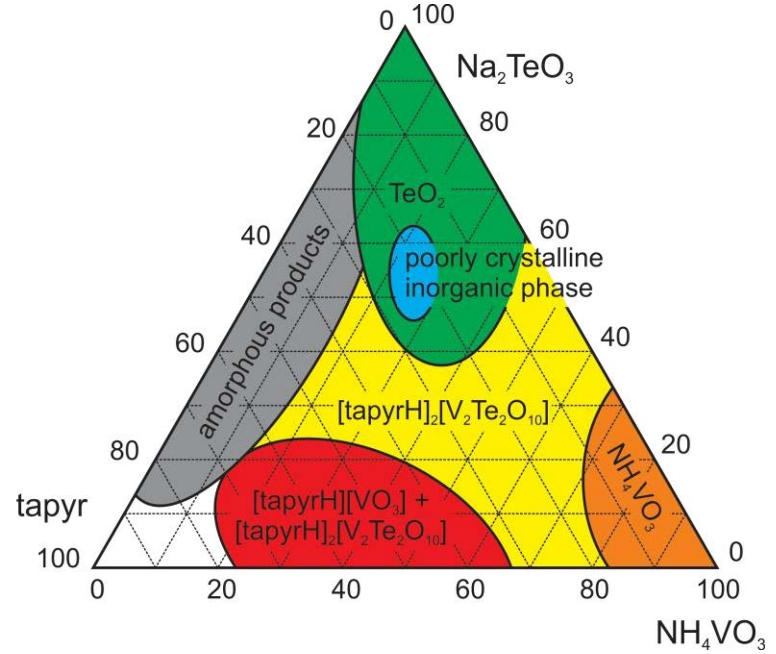

Figure 1. Composition space diagram for the NH_4VO_3 / Na_2TeO_3 / tapyr / H_2O system.

Two organically templated metal oxides are observed in the composition space diagram for the NH_4VO_3 / Na_2TeO_3 / tapyr / H_2O system. $[C_4H_8N_5][VO_3]$ (**1**) contains protonated $[tapyrH]^+$ cations and one-dimensional $[V^{5+}O_{2/2}O_{2/1}]_n^{n-}$ chains. $[C_4H_8N_5]_2[V_2Te_2O_{10}]$ is constructed from $[tapyrH]^+$ cations and two-dimensional $[V_2Te_2O_{10}]_n^{2n-}$ layers. The $[V^{5+}O_{2/2}O_{2/1}]_n^{n-}$ chains found in **1** are shown in Figure 2. One unique V^{5+} center is present, with V=O and V-$O_{bridging}$ bond ranges of 1.635(3) to 1.654(3) Å and 1.790(3) and 1.812(3) Å, respectively. Similar metavanadate chains have been reported previously.[53-60] The chains in **1** run parallel to one another, with $[tapyrH]^+$ cations residing between vanadate chains (see Figure 3). Extensive hydrogen-bonding is observed between the organic cations and inorganic chains. $[C_4H_8N_5]_2[V_2Te_2O_{10}]$ (**2**) contains $[V_2Te_2O_{10}]_n^{2n-}$ layers that are built from Te_2O_2 dimers, which are in turn connected to one another through $[VO_4]$ bridges (see Figure 4). The tellurium dimers are arranged in a herringbone pattern. The $[tapyrH]^+$ cations stack roughly perpendicular to the $[V_2Te_2O_{10}]_n^{2n-}$ layers, as shown in Figure

5. Again, an extensive hydrogen-bonding network is observed between the organic cations and inorganic layers.

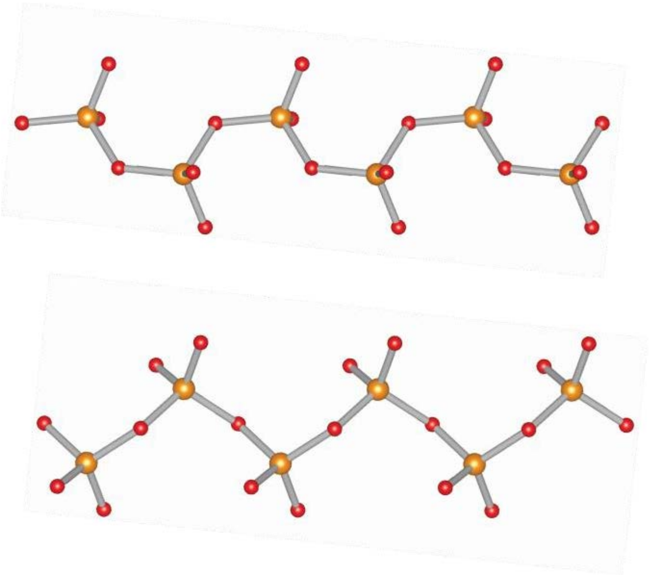

Figure 2. Ball-and-stick representations of the $[VO_3]_n^{n-}$ chains in $[C_4H_8N_5][VO_3]$ (**1**). Orange and red spheres represent vanadium and oxygen, respectively.

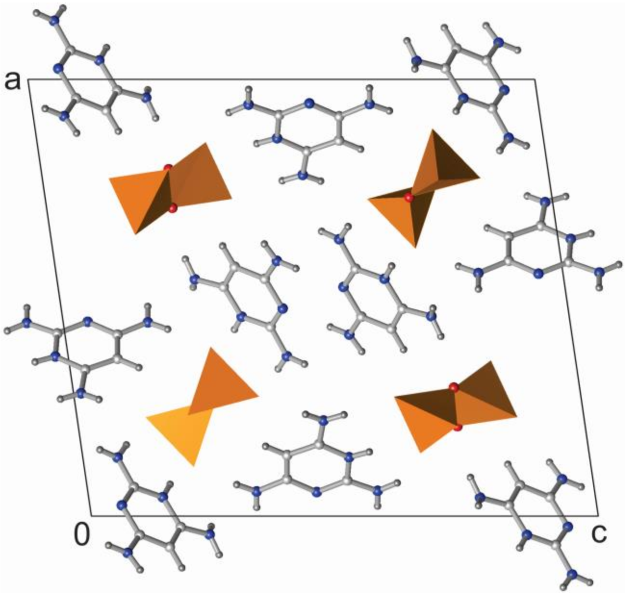

Figure 3. Three-dimensional packing figure of $[C_4H_8N_5][VO_3]$ (**1**). Orange polyhedra represent $[VO_4]$, while red, blue, white and grey spheres represent oxygen, nitrogen, carbon and hydrogen respectively.

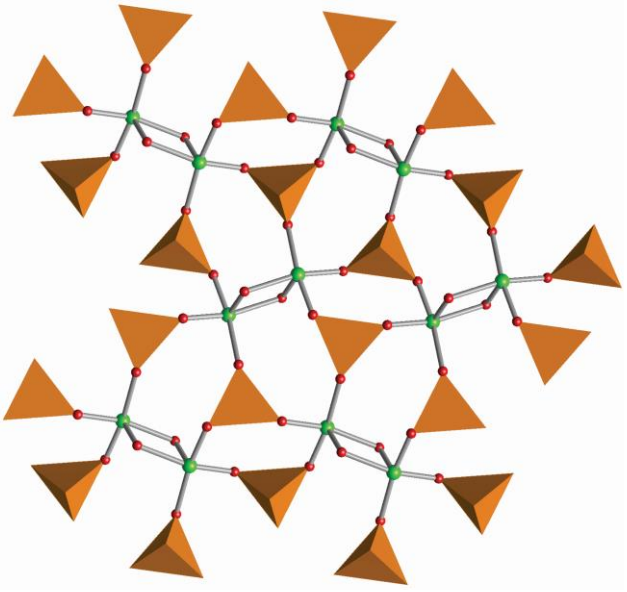

Figure 4. $[V_2Te_2O_{10}]_n^{2n-}$ layers in $[C_4H_8N_5]_2[V_2Te_2O_{10}]$ (**2**). Orange polyhedra

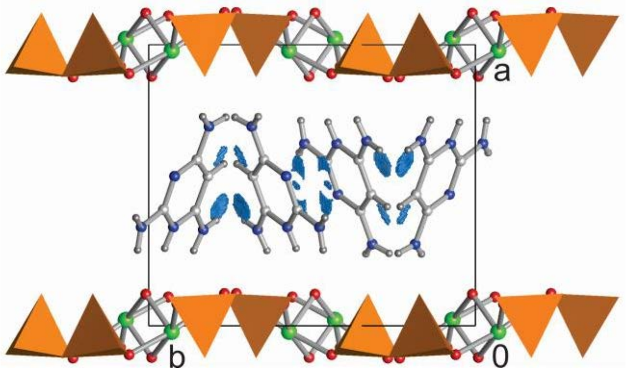

Figure 5. Three-dimensional packing figure $[C_4H_8N_5]_2[V_2Te_2O_{10}]$ (**2**). Orange polyhedra represent

represent $[VO_4]$, while green and red spheres represent tellurium and oxygen, respectively.

$[VO_4]$, while green, red, blue, white and grey spheres represent tellurium, oxygen, nitrogen, carbon and hydrogen respectively. Blue isosurfaces represent inter-cation attractions from the NCI calculations.

The crystallization field positions for compounds **1** and **2** are largely dictated by their compositions. $[C_4H_8N_5][VO_3]$ (**1**), which does not contain any tellurium, is found only in regions of low tellurium concentration. As the Te concentration increases, $[C_4H_8N_5]_2[V_2Te_2O_{10}]$ (**2**) begins to dominate crystallization. Inorganic-only phases are also found under conditions of either very high tellurium concentrations (TeO_2) or very low tapyr concentrations (NH_4VO_3), where either solubility limits force precipitation of TeO_2 or low amine concentrations preclude the formation of an organically templated material.

The $[V_2Te_2O_{10}]_n^{2n-}$ layers found in $[C_4H_8N_5]_2[V_2Te_2O_{10}]$ (**2**) are similar to two other vanadium tellurite layer connectivities (see Figure 6). These layers are found in $[C_6H_{16}N_2][V_2Te_2O_{10}]$[27] and $[C_5H_{14}N_2][V_2Te_2O_{10}]$,[27] which contain 2,5-dimethylpiperazine and 2-methylpiperazine, respectively. The similarities between the layers in $[C_4H_8N_5]_2[V_2Te_2O_{10}]$ (**2**), $[C_6H_{16}N_2][V_2Te_2O_{10}]$ and $[C_5H_{14}N_2][V_2Te_2O_{10}]$, despite strong differences in amine properties, prompted a deeper analysis of the factors governing layer formation in these materials. Structures of the amines in these three compounds are shown in Figure 7.

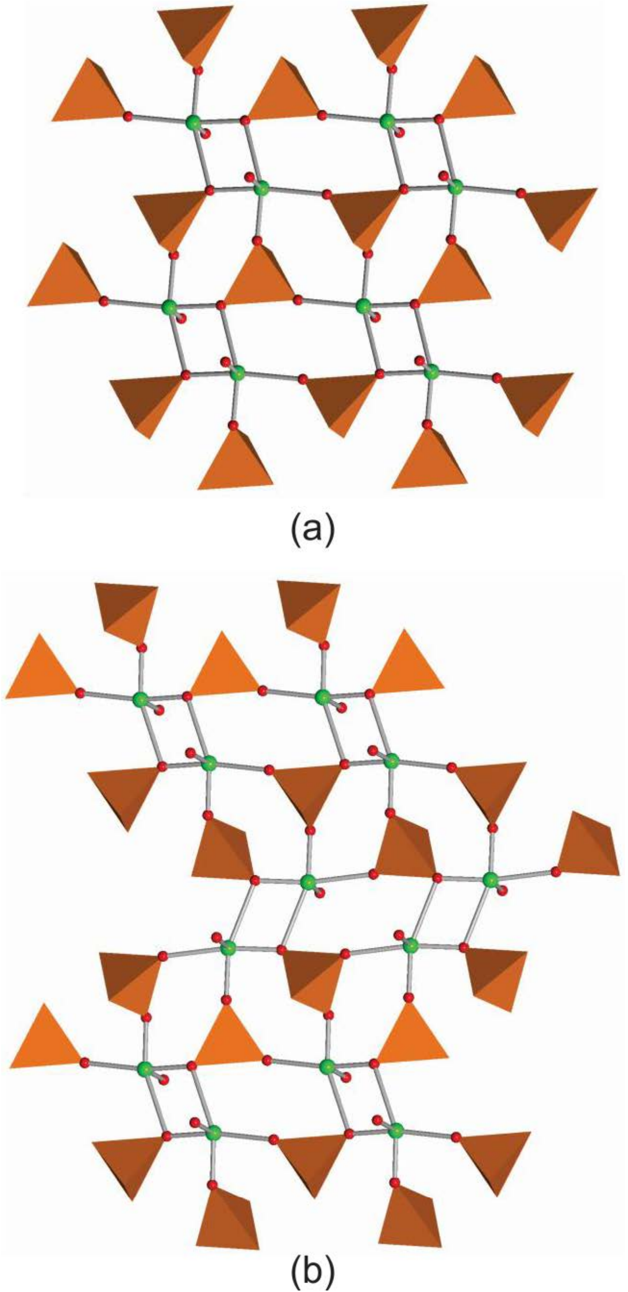

Figure 6. $[V_2Te_2O_{10}]_n^{2n-}$ layers in (a) $[C_6H_{16}N_2][V_2Te_2O_{10}]$ and (b) $[C_5H_{14}N_2][V_2Te_2O_{10}]$. Orange polyhedra represent $[VO_4]$, while green and red spheres represent tellurium and oxygen, respectively.

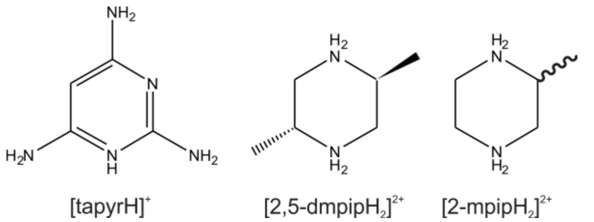

Figure 7. Structures of $[\text{tapyrH}]^+$, $[\text{2,5-dmpipH}_2]^{2+}$ and $[\text{2-mpipH}_2]^{2+}$.

We have investigated and articulated a hierarchy of influences that dictate the structure and composition of organically templated metal oxides. This work, based on efforts by Ferey,[7, 61] Rao,[15, 62-64] and others,[17, 65] has led to the articulation of influences of differing strength and importance. The *primary influence* is constructed from the relative concentrations of the reactive species present in each reaction,[20, 23-24, 27, 48-50, 66-69] and dictates the identities and relative ratios of the primary building units available for further reaction. The positions of the respective crystallization fields indicate the regions of phase stability. The *secondary influence* is charge density matching between the cationic organic component and the anionic inorganic component. The formation of larger secondary building units enables the charge density of the inorganic structures to match that of the organic cations.[27, 70-71] A range of *tertiary influences* exist, which affect local bonding interactions and symmetry but do not control larger stoichiometries or connectivities. Examples include hydrogen-bonding effects,[27, 72-73] sterics[5, 73] and symmetry.[26, 74-77] A full analysis of these influences was conducted in order to more fully understand the differences in layer tessellation between $[C_4H_8N_5]_2[V_2Te_2O_{10}]$ (**2**), $[C_6H_{16}N_2][V_2Te_2O_{10}]$ and $[C_5H_{14}N_2][V_2Te_2O_{10}]$.

The composition space diagram for the NH_4VO_3 / Na_2TeO_3 / tapyr / H_2O is shown in Figure 1, while analogous diagrams for the $NaVO_3$ / Na_2TeO_3 / 2,5-dimethylpiperazine / H_2O and $NaVO_3$ / Na_2TeO_3 / 2-methylpiperazine / H_2O are shown in Figure S1, in Appendix A. The differences among these composition space diagrams are largely manifest in two ways. The use of $NaVO_3$ in the 2,5-dimethylpiperazine (2,5-dmpip) and 2-methylpiperazine (2-mpip) systems causes increased Na^+ concentrations with respect to the tapyr system. The observation of $NaVTeO_5$ crystallization fields when using 2,5-dmpip and 2-mpip is attributed to the increased Na^+ concentration in these two systems. The decreased Na^+ concentration in the taypr system destabilizes $NaVTeO_5$, and leads to an expansion of the $[C_4H_8N_5]_2[V_2Te_2O_{10}]$ (**2**) crystallization field into higher Te concentrations. Second, the presence of a tellurium-free organically templated vanadate, $[C_4H_8N_5][VO_3]$ (**1**), when using only tapyr, suggests that the differences in amine properties directly affect compound stabilities.

The $[V_2Te_2O_{10}]_n^{2n-}$ layers in $[C_4H_8N_5]_2[V_2Te_2O_{10}]$ (**2**), $[C_6H_{16}N_2][V_2Te_2O_{10}]$ and $[C_5H_{14}N_2][V_2Te_2O_{10}]$ are constructed from the same secondary building units, namely $[Te_2O_2]$ dimers that are connected to one another through bridging $[VO_4]$ groups. The structures of these dimers and tetrahedral building units are largely dictated by the reactions conditions as speciation is dependent upon experimental factors such as pH, concentration and temperature. As discussed above, the way in which these building units form larger structures involves charge density matching between the cationic and anionic components. The formation of neutral ammonium – secondary building unit pairs allows for infinite condensation and crystallization. The charge densities of the inorganic components change as the structures evolve from isolated building units to larger structures, while the charge densities of the organic components are fixed by protonation states and pK_as. Probing the role of charge density matching involves calculating both the charges and surface areas of the inorganic species. See Table 2.

The surface areas of the $[V_2Te_2O_{10}]_n^{2n-}$ layers in $[C_4H_8N_5]_2[V_2Te_2O_{10}]$ (**2**), $[C_6H_{16}N_2][V_2Te_2O_{10}]$ and $[C_5H_{14}N_2][V_2Te_2O_{10}]$ were calculated using the rolling sphere approach described by Richards *et al.*,[39] see above. The surface areas of $[C_4H_8N_5]_2[V_2Te_2O_{10}]$ and $[C_6H_{16}N_2][V_2Te_2O_{10}]$ are nearly identical, while only a small increase is observed for $[C_5H_{14}N_2][V_2Te_2O_{10}]$. This suggests that surface areas are not responsible for the observed layer tessellation differences between **2**, $[C_6H_{16}N_2][V_2Te_2O_{10}]$ and $[C_5H_{14}N_2][V_2Te_2O_{10}]$. The anion charges were calculated using Iterative Hirshfeld (IH) partial atomic charges,[43-44] as described above. Larger differences are observed in the charges, with a difference of ~18 % between $[C_4H_8N_5]_2[V_2Te_2O_{10}]$ (**2**) and $[C_5H_{14}N_2][V_2Te_2O_{10}]$. These differences most likely result from electron density variations in the IH charge partitioning scheme. As noted above, the inorganic components have the same stoichiometries, identical SBUs and similar, but distinctly different tessellation patterns. As such, the differences in layer tessellation patterns do not come from either primary or secondary influences. An investigation of the tertiary influences was performed by probing the interactions between the cationic and anionic components of these structures.

The organic amines present in compound **2** differ distinctly from those in $[C_6H_{16}N_2][V_2Te_2O_{10}]$ and $[C_5H_{14}N_2][V_2Te_2O_{10}]$ (see Figure 7). First, the 2,4,6-triaminopyrimidine (tapyr) cations in **2** exist as singly protonated $[C_4H_8N_5]^+$ cations, while the 2,5-dmpip and 2-mpip cations in $[C_6H_{16}N_2][V_2Te_2O_{10}]$ and $[C_5H_{14}N_2][V_2Te_2O_{10}]$, respectively are both doubly protonated as $[C_6H_{16}N_2]^{2+}$ and $[C_5H_{14}N_2]^{2+}$. Second, $[\text{tapyrH}]^+$ is planar and can participate in π-π stacking interactions, while rings in $[2,5\text{-dmpipH}_2]^{2+}$ and $[2\text{-mpipH}_2]^{2+}$ cannot. Third, $[\text{tapyrH}]^+$ contains four neutral ammonium sites, while both ammonium sites in $[2,5\text{-dmpipH}_2]^{2+}$ and in $[2\text{-mpipH}_2]^{2+}$ are fully protonated. Finally, $[2,5\text{-dmpipH}_2]^{2+}$ and $[2\text{-mpipH}_2]^{2+}$ each contain many carbon hydrogen bonds, capable of creating an extensive C-H $\cdots$ O hydrogen-bonding network. The importance of C-H $\cdots$ O hydrogen-bonding in this type of chemistry has been well established. The $[\text{tapyrH}]^+$ cations in **2**, in contrast, contain only a single C-H bond each, which limits the possible extent of such interactions.

The charges on the protonated organic amines in **2**, $[C_6H_{16}N_2][V_2Te_2O_{10}]$ and $[C_5H_{14}N_2][V_2Te_2O_{10}]$ affect the overall stoichiometry of the resulting compounds. The amine : $[V_2Te_2O_{10}]$ ratios are 2 : 1 for **2** and 1 : 1 for $[C_6H_{16}N_2][V_2Te_2O_{10}]$ and $[C_5H_{14}N_2][V_2Te_2O_{10}]$. As noted above, the inorganic layer surface areas do not differ substantially among these three compounds, suggesting that stoichiometry does not play a pivotal roles in the layer tessellation. Instead, one must look to the other differences in amine structure and their interactions within the compounds. Noncovalent interaction (NCI) analyses[78-80] are effective for elucidating the role of all noncovalent interactions, both attractive and repulsive, in the formation of organically templated metal oxides.[19-20] The NCI fingerprint for compound **2** is shown in Figure 8, while fingerprints for $[C_6H_{16}N_2][V_2Te_2O_{10}]$ and $[C_5H_{14}N_2][V_2Te_2O_{10}]$ are provided in Appendix A (Figure S2 and Figure S3).

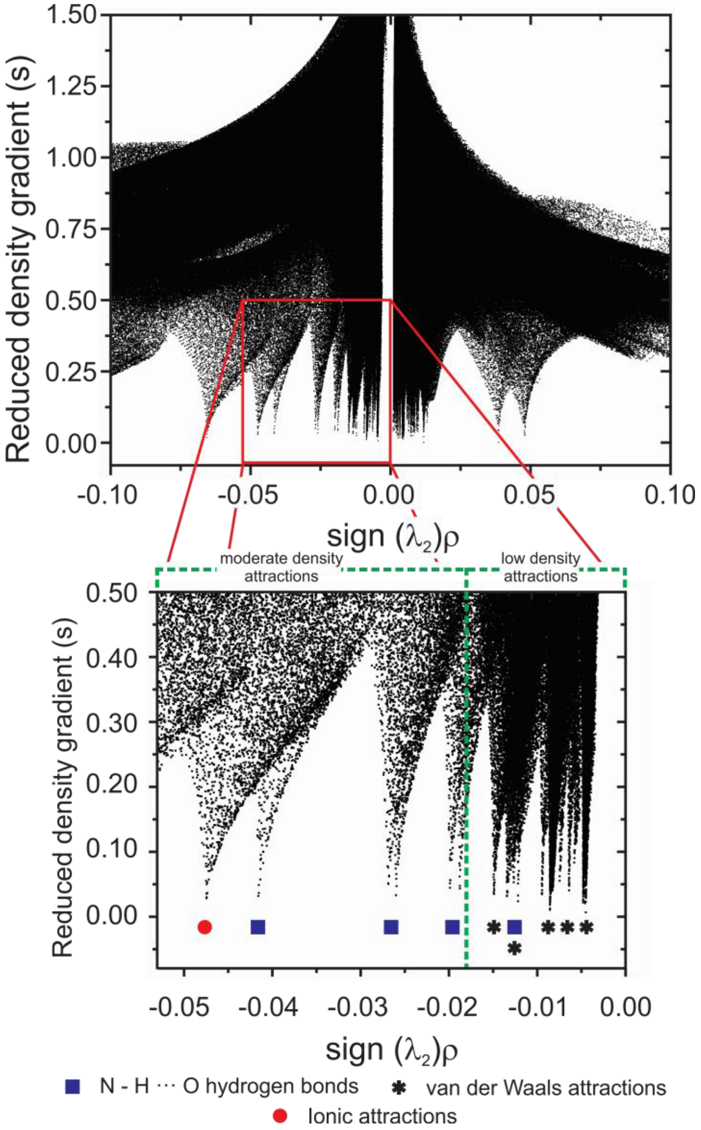

Figure 8. NCI analysis of $[C_4H_8N_5]_2[V_2Te_2O_{10}]$ (**2**).

NCI analyses allow for one to identify, quantify, and visualize all noncovalent interactions in a given structure. Each peak in the NCI fingerprints corresponds to a single interaction, with attractive interactions appearing at negative sign(λ_2)ρ values. Isosurfaces were generated for all peaks between -0.10 and 0.10 in sign(λ_2)ρ to identify the nature of each individual interaction (see Figure 8). Inspection of the NCI fingerprints for **2**, [$C_6H_{16}N_2$][$V_2Te_2O_{10}$] and [$C_5H_{14}N_2$][$V_2Te_2O_{10}$] reveals both similarities and differences. The low density interactions in all three compounds appear at sign(λ_2)ρ values below -0.018. These interactions correspond to C-H ··· O hydrogen bonds, and van der Waals and dispersion type interactions. The moderate density attractions, N-H ··· O hydrogen bonds and weak ionic interactions, are found below -0.053. The regions designated as moderate density and low density attractions are shown in Figure 8.

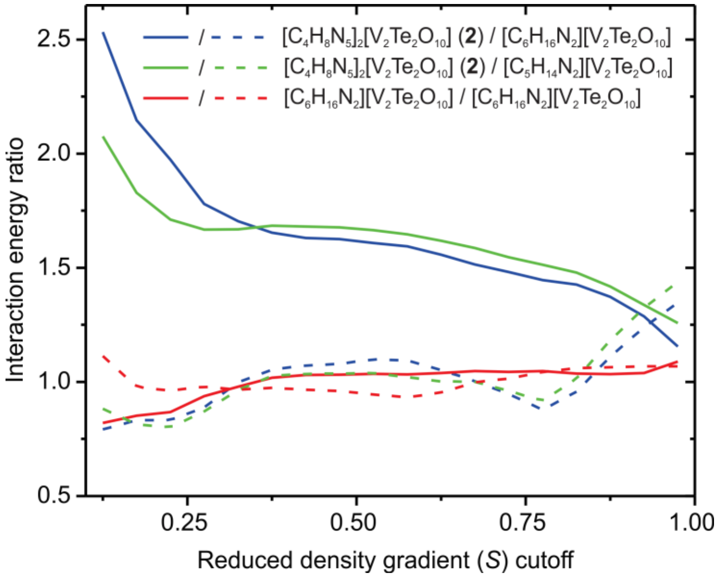

Figure 9. Interaction energy ratios as a function of reduced density gradient cutoff. Solid lines represent low-density attractions while dashed lines represent moderate density attractions.

The relative contributions of the different types of noncovalent interactions can be quantified by integrating the NCI datapoints. The cutoffs identified above (-0.053 to -0.018 for moderate and -0.018 to 0 for low electron density attractions) were used in NCI integrations. These numerical integrations used a cubic grid with 0.1 au increments, as described earlier.[19] Interaction energy ratios between **2**, [$C_6H_{16}N_2$][$V_2Te_2O_{10}$] and [$C_5H_{14}N_2$][$V_2Te_2O_{10}$] are shown in Figure 9.

Ratios of moderate density attractions are shown as dashed lines, while low density attraction ratios use solid lines. The relative interaction energy ratios for moderate density attractions are effectively 1 for all ratio combinations, suggesting that the relative strengths of the moderate density attractions are comparable among compounds and are not the source of layer tessellation differences. In contrast, the relative interaction energy ratios for low density attractions between compound **2** and either $[C_6H_{16}N_2][V_2Te_2O_{10}]$ or $[C_5H_{14}N_2][V_2Te_2O_{10}]$ deviate distinctly from 1. This indicates that the low density attractions in compound **2** are significantly stronger than in either $[C_6H_{16}N_2][V_2Te_2O_{10}]$ or $[C_5H_{14}N_2][V_2Te_2O_{10}]$. It should be noted that the low density interaction energy ratio for $[C_6H_{16}N_2][V_2Te_2O_{10}]$: $[C_5H_{14}N_2][V_2Te_2O_{10}]$ is approximately 1. The increased strength of the low density attractions in compound **2** when compared to $[C_6H_{16}N_2][V_2Te_2O_{10}]$ and $[C_5H_{14}N_2][V_2Te_2O_{10}]$ largely comes from π - π stacking interactions between adjacent $[\text{tapyrH}]^+$ cations. We are able to attribute the increased low density attraction strength in compound **2** to π - π stacking because such interactions do not exist in $[C_6H_{16}N_2][V_2Te_2O_{10}]$ and $[C_5H_{14}N_2][V_2Te_2O_{10}]$. There is a large decrease in the number of C-H $\cdots$ O hydrogen bonds in **2** and isosurfaces corresponding to the π - π stacking in **2** can be visualized (see Figure 10). Both parallel displaced and t-shaped interactions are observed.[81]

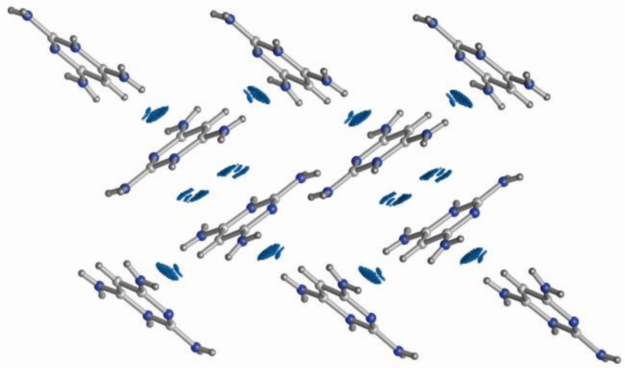

Figure 10. Ball-and-stick representation of the cation structure in $[C_4H_8N_5]_2[V_2Te_2O_{10}]$ (**2**). Blue, white and grey spheres represent nitrogen, carbon and hydrogen, respectively. Blue isosurfaces represent inter-cation attractions from the NCI calculations.

The presence of π - π stacking interactions between adjacent $[\text{tapyrH}]^+$ cations in $[C_4H_8N_5]_2[V_2Te_2O_{10}]$ (**2**) strongly contributes to these organic cations being aligned in a perpendicular fashion with respect to the $[V_2Te_2O_{10}]_n^{2n-}$ layers (see Figure 5). This cation geometry allows for the majority of the N-H bonds to be oriented in a way that maximizes N-H ··· O hydrogen-bonding to the inorganic layers. Together, these two influences dictate cation orientation. The positions of the N-H groups on the $[\text{tapyrH}]^+$ cations affect the inorganic layers. As discussed above, no significant differences in charge density matching were observed between compound **2**, $[C_6H_{16}N_2][V_2Te_2O_{10}]$ and $[C_5H_{14}N_2][V_2Te_2O_{10}]$. As such, the differences in layer tessellation must be ascribed to weaker tertiary influences. The π - π stacking interactions drive cation orientation, which in turn affect the positions of hydrogen bond acceptors.

The differences in the $[V_2Te_2O_{10}]_n^{2n-}$ layers in compound **2**, $[C_6H_{16}N_2][V_2Te_2O_{10}]$ and $[C_5H_{14}N_2][V_2Te_2O_{10}]$ are most clearly observed in the apical positions on the $[TeO_5]$ square pyramids. These positions are occupied by terminal oxide anions in $[C_6H_{16}N_2][V_2Te_2O_{10}]$ and $[C_5H_{14}N_2][V_2Te_2O_{10}]$, as shown in Figure 6. In contrast, each apical oxide anion in compound **2** bridges to an adjacent tellurium center (see Figure 4). A corresponding shift in bond metrics is observed, with the Te – O_{apical} bond length increasing to 1.6455(17) Å in **2** from 1.620(2) and 1.6124(18) Å in $[C_6H_{16}N_2][V_2Te_2O_{10}]$ and $[C_5H_{14}N_2][V_2Te_2O_{10}]$, respectively. The largest difference is observed within the shared edge in the tellurium dimer. The longest distance in this dimer in **2** is 2.3159(16) Å, while analogous distances in $[C_6H_{16}N_2][V_2Te_2O_{10}]$ and $[C_5H_{14}N_2][V_2Te_2O_{10}]$ are 2.7010(19) and 2.6710(15) Å, respectively. The bond metrics affect the relative nucleophilicities of the oxide anions, as determined using bond valence sums. The result of which is that more oxide anions exhibit higher nucleophilicities, making them better able to accept hydrogen bonds from the $[tapyrH]^+$ cations. Moreover, the positions of these oxide anions are aligned with the hydrogen donor cations in the interlayer spacing.

3. Conclusions

The formation of organically templated metal oxides, such as $[C_4H_8N_5][VO_3]$ (**1**) and $[C_4H_8N_5]_2[V_2Te_2O_{10}]$ (**2**), is governed by a series of influences of differing strengths. The crystallization fields for compounds **1** and **2** are dictated by the relative reactant concentrations, with the tellurium concentration acting as a primary determinant to product identity. The layer tessellation in compound **2** is influenced directly by the organic amine structure, which is in turn controlled by π - π stacking interactions. These weak interactions play a pivotal role in directing the larger three-dimensional structure in this compound, as observed using noncovalent interaction (NCI) indices.

Acknowledgements

The authors acknowledge support from the NSF (DMR-1709351), A.N. and J.S. acknowledge the Henry Dreyfus Teacher-Scholar Awards Program. M.Z. acknowledges support for the purchase of a diffractometer from the NSF grant CHE 0087210, the Ohio Board of Regents grant CAP-491 and from Youngstown State University.

Appendix A. Supporting information

Crystallographic data for the structures reported in this paper have been deposited with the Cambridge Crystallographic Data Centre as supplementary publication numbers 1885026 and 1885027. Composition space diagrams for the $NaVO_3$ / Na_2TeO_3 / 2,5-dmpip and $NaVO_3$ / Na_2TeO_3 / 2-mpip systems, NCI analyses for $[C_6H_{16}N_2][V_2Te_2O_{10}]$ and $[C_5H_{14}N_2][V_2Te_2O_{10}]$, three-dimensional packing figures for $[C_4H_8N_5]_2[V_2Te_2O_{10}]$ (**2**), $[C_6H_{16}N_2][V_2Te_2O_{10}]$ and $[C_5H_{14}N_2][V_2Te_2O_{10}]$, tables of bond valences sums for $[C_4H_8N_5][VO_3]$ (**1**), $[C_4H_8N_5]_2[V_2Te_2O_{10}]$ (**2**), $[C_6H_{16}N_2][V_2Te_2O_{10}]$ and $[C_5H_{14}N_2][V_2Te_2O_{10}]$, and calculated Iterative-Hirshfeld partial atomic charges for $[C_4H_8N_5]_2[V_2Te_2O_{10}]$ (**2**) are available.

Table 1. Crystallographic data for compounds **1** and **2**.

Compound	$[C_4H_8N_5][VO_3]$ (**1**)	$[C_4H_8N_5]_2[V_2Te_2O_{10}]$ (**2**)
Formula	$C_4H_8N_5O_3V$	$C_8H_{16}N_{10}O_{10}Te_2V_2$
fw	225.08	769.36
Space-Group	$P2_1/n$ (no. 14)	$P2_1/c$ (no. 14)
a / Å	16.7364(11)	10.3944(16)
b / Å	5.1963(2)	12.0324(18)
c / Å	19.2225(10)	8.1768(12)
α / °	90	90
β / °	98.271(5)	94.768(2)
γ / °	90	90
V / Å^3	1654.34(9)	1019.13(15)
Z	8	2
ρ_{calc} / g cm^{-3}	1.807	2.507
λ / Å	1.54180	0.71073
T / K	100(1)	100(1)
μ / mm^{-1}	9.982	3.796
$R_{1,}$[a]	0.0513	0.0238
wR_2[b]	0.1400	0.550

[a] $R_1 = \Sigma \| F_o | - | F_c \| / \Sigma | F_o |$. [b] $wR_2 = [\Sigma w(F_o^2 - F_c^2)^2 / [\Sigma w(F_o^2)^2]^{1/2}$.

Table 2. Surface area and charge density results for the $[V_2Te_2O_{10}]_n^{2n-}$ layers in compound **2**, $[C_6H_{16}N_2][V_2Te_2O_{10}]$[27] and $[C_5H_{14}N_2][V_2Te_2O_{10}]$.[27]

Compound	**Surface area (Å^2)**	**Anion Charge**	**Charge density (e Å^{-2})**
$[C_6H_{16}N_2][V_2Te_2O_{10}]$	107.81	-1.1554	-0.01086
$[C_5H_{14}N_2][V_2Te_2O_{10}]$	119.23	-1.2308	-0.01104
$[C_4H_8N_5]_2[V_2Te_2O_{10}]$ (**2**)	107.61	-1.0362	-0.00962

Figure captions.

Figure 1. Composition space diagram for the NH_4VO_3 / Na_2TeO_3 / tapyr / H_2O system.

Figure 2. Ball-and-stick representations of the $[VO_3]_n^{n-}$ chains in $[C_4H_8N_5][VO_3]$ (**1**). Orange and red spheres represent vanadium and oxygen, respectively.

Figure 3. Three-dimensional packing figure of $[C_4H_8N_5][VO_3]$ (**1**). Orange polyhedra represent $[VO_4]$, while red, blue, white and grey spheres represent oxygen, nitrogen, carbon and hydrogen respectively.

Figure 4. $[V_2Te_2O_{10}]_n^{2n-}$ layers in $[C_4H_8N_5]_2[V_2Te_2O_{10}]$ (**2**). Orange polyhedra represent $[VO_4]$, while green and red spheres represent tellurium and oxygen, respectively.

Figure 5. Three-dimensional packing figure $[C_4H_8N_5]_2[V_2Te_2O_{10}]$ (**2**). Orange polyhedra represent $[VO_4]$, while green, red, blue, white and grey spheres represent tellurium, oxygen, nitrogen, carbon and hydrogen respectively. Blue isosurfaces represent inter-cation attractions from the NCI calculations.

Figure 6. $[V_2Te_2O_{10}]_n^{2n-}$ layers in (a) $[C_6H_{16}N_2][V_2Te_2O_{10}]$ and (b) $[C_5H_{14}N_2][V_2Te_2O_{10}]$. Orange polyhedra represent $[VO_4]$, while green and red spheres represent tellurium and oxygen, respectively.

Figure 7. Structures of $[\text{tapyrH}]^+$, $[\text{2,5-dmpipH}_2]^{2+}$ and $[\text{2-mpipH}_2]^{2+}$.

Figure 8. NCI analysis of $[C_4H_8N_5]_2[V_2Te_2O_{10}]$ (**2**).

Figure 9. Interaction energy ratios as a function of reduced density gradient cutoff. Solid lines represent low-density attractions while dashed lines represent moderate density attractions.

Figure 10. Ball-and-stick representation of the cation structure in $[C_4H_8N_5]_2[V_2Te_2O_{10}]$ (**2**). Blue, white and grey spheres represent nitrogen, carbon and hydrogen, respectively. Blue isosurfaces represent inter-cation attractions from the NCI calculations.

For Graphical Abstract use only

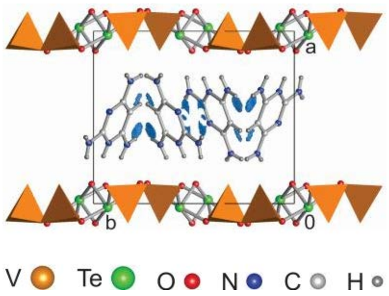

1. Li, B.; Wen, H.-M.; Zhou, W.; Chen, B., *The Journal of Physical Chemistry Letters* **2014,** *5*, 3468-3479.
2. Jiang, J.; Furukawa, H.; Zhang, Y.-B.; Yaghi, O. M., *J. Am. Chem. Soc.* **2016,** *138*, 10244-10251.
3. Snaith, H. J., *Nature Materials* **2018,** *17*, 372-376.
4. Haag, W. O., *Stud. Surf. Sci. Catal.* **1994,** *84*, 1375-94.
5. Glor, E. C.; Blau, S. M.; Yeon, J.; Zeller, M.; Shiv Halasyamani, P.; Schrier, J.; Norquist, A. J., *J. Solid State Chem.* **2011,** *184*, 1445-1450.
6. Cundy, C. S.; Cox, P. A., *Chem. Rev.* **2003,** *103*, 663-701.
7. Ferey, G., *J. Fluorine Chem.* **1995,** *72*, 187-93.
8. Rao, C. N. R.; Natarajan, S.; Neeraj, S., *J. Am. Chem. Soc.* **2000,** *122*, 2810-2817.
9. Rabenau, A., *Angew. Chem. Int. Ed.* **1985,** *24*, 1026-1040.
10. Yu, J.; Xu, R., *Acc. Chem. Res.* **2010,** *43*, 1195-1204.
11. Price, S. L., *Acc. Chem. Res.* **2009,** *42*, 117-126.
12. Day, G. M.; Cooper, T. G.; Cruz-Cabeza, A. J.; Hejczyk, K. E.; Ammon, H. L.; Boerrigter, S. X. M.; Tan, J. S.; Della Valle, R. G.; Venuti, E.; Jose, J.; Gadre, S. R.; Desiraju, G. R.; Thakur, T. S.; van Eijck, B. P.; Facelli, J. C.; Bazterra, V. E.; Ferraro, M. B.; Hofmann, D. W. M.; Neumann, M. A.; Leusen, F. J. J.; Kendrick, J.; Price, S. L.; Misquitta, A. J.; Karamertzanis, P. G.; Welch, G. W. A.; Scheraga, H. A.; Arnautova, Y. A.; Schmidt, M. U.; van de Streek, J.; Wolf, A. K.; Schweizer, B., *Acta Crystallogr., Sect. B Struct. Sci.* **2009,** *B65*, 107-125.
13. Mellot-Draznieks, C., *J. Mater. Chem.* **2007,** *17*, 4348-4358.
14. Lonie, D. C.; Zurek, E., *Comput. Phys. Commun.* **2010,** *182*, 372-387.
15. Rao, C. N. R.; Dan, M.; Behera, J. N., *Pure Appl. Chem.* **2005,** *77*, 1655-1674.
16. Cheetham, A. K.; Rao, C. N. R., *MRS Bull.* **2005,** *30*, 93-98.
17. Marvel, M. R.; Pinlac, R. A. F.; Lesage, J.; Stern, C. L.; Poeppelmeier, K. R., *Z. Anorg. Allg. Chem.* **2009,** *635*, 869-877.
18. Chang, K. B.; Vinokur, A.; Pinlac, R. A. F.; Suchomel, M. R.; Marvel, M. R.; Poeppelmeier, K. R., *Inorg. Chem.* **2014,** *53*, 6979-6984.
19. Nourmahnad, A.; Smith, M. D.; Zeller, M.; Ferrence, G. M.; Schrier, J.; Norquist, A. J., *Inorg. Chem.* **2015,** *54*, 694-703.
20. Nourmahnad, A.; Wenny, M. B.; Zeller, M.; Schrier, J.; Norquist, A. J., *J. Solid State Chem.* **2016,** *236*, 215-221.
21. Adler, P.; Falk, C.; Friedler, S. A.; Rybeck, G.; Scheidegger, C.; Smith, B.; Venkatasubramanian, S. In *Auditing Black-box Models for Indirect Influence*, Proceedings of the IEEE International Conference on Data Mining, 2016.
22. Adler, P. D. F.; Xu, R.; Olshansky, J. H.; Smith, M. D.; Elbert, K. C.; Yang, Y.; Ferrence, G. M.; Zeller, M.; Schrier, J.; Norquist, A. J., *Polyhedron* **2016,** *114*, 184-193.
23. Olshansky, J. H.; Wiener, K. J.; Smith, M. D.; Nourmahnad, A.; Charles, M. J.; Zeller, M.; Schrier, J.; Norquist, A. J., *Inorg. Chem.* **2014,** *53*, 12027-12035.
24. Norquist, A. J.; Heier, K. R.; Stern, C. L.; Poeppelmeier, K. R., *Inorg. Chem.* **1998,** *37*, 6495-6501.
25. Halasymani, P. S.; Heier, K. R.; Norquist, A. J.; Stern, C. L.; Poeppelmeier, K. R., *Inorg. Chem.* **1998,** *37*, 369-371.
26. Choyke, S. J.; Blau, S. M.; Larner, A. A.; Narducci Sarjeant, A.; Yeon, J.; Halasyamani, P. S.; Norquist, A. J., *Inorg. Chem.* **2009,** *48*, 11277-11282.

27. Smith, M. D.; Blau, S. M.; Chang, K. B.; Zeller, M.; Schrier, J.; Norquist, A. J., *Cryst. Growth Des.* **2011,** *11*, 4213-4219.
28. Rigaku Corp.: The Woodlands, TX, USA.
29. Otwinowski, Z.; Minor, W., Processing of X-ray diffraction data collected in oscillation mode. In *Methods Enzymol.*, Academic Press: 1997; Vol. 276, pp 307-326.
30. *Apex2 v2009.7-0.*, Bruker AXS Inc.: Madison (WI), USA, 2009.
31. Altomare, A.; Cascarano, G.; Giacovazzo, C.; Guagliardi, A., *J. Appl. Crystallogr.* **1993,** *26*, 343-50.
32. Betteridge, P. W.; Carruthers, J. R.; Cooper, R. I.; Prout, K.; Watkin, D. J., *J. Appl. Crystallogr.* **2003,** *36*, 1487.
33. Dowty, E. *ATOMS v. 6.0*, Shape Software: TN, USA,, 2002.
34. Brown, I. D.; Altermatt, D., *Acta Crystallogr. Sect. B* **1985,** *41*, 244-7.
35. Brese, N. E.; O'Keeffe, M., *Acta Crystallogr. Sect. B* **1991,** *47*, 192-7.
36. Gonze, X.; Beuken, J. M.; Caracas, R.; Detraux, F.; Fuchs, M.; Rignanese, G. M.; Sindic, L.; Verstraete, M.; Zerah, G.; Jollet, F.; Torrent, M.; Roy, A.; Mikami, M.; Ghosez, P.; Raty, J. Y.; Allan, D. C., *Comput. Mater. Sci.* **2002,** *25*, 478-492.
37. Gonze, X.; Amadon, B.; Anglade, P. M.; Beuken, J. M.; Bottin, F.; Boulanger, P.; Bruneval, F.; Caliste, D.; Caracas, R.; Cote, M.; Deutsch, T.; Genovese, L.; Ghosez, P.; Giantomassi, M.; Goedecker, S.; Hamann, D. R.; Hermet, P.; Jollet, F.; Jomard, G.; Leroux, S.; Mancini, M.; Mazevet, S.; Oliveira, M. J. T.; Onida, G.; Pouillon, Y.; Rangel, T.; Rignanese, G. M.; Sangalli, D.; Shaltaf, R.; Torrent, M.; Verstraete, M. J.; Zerah, G.; Zwanziger, J. W., *Comput. Phys. Commun.* **2009,** *180*, 2582-2615.
38. Momma, K.; Izumi, F., *J. Appl. Crystallogr.* **2008,** *41*, 653-658.
39. Richards, F. M., *Ann. Rev. Biophys. Bioeng.* **1977,** *6*, 151-76.
40. Huang, C. *DMS.*, Computer Graphics Lab, University of California, San Francisco, CA, USA: 2002.
41. Andersson, S.; Astrom, A.; Galy, J.; Meunier, G., *J. Solid State Chem.* **1973,** *6*, 187-90.
42. Galy, J.; Meunier, G.; Andersson, S.; Astrom, A., *J. Solid State Chem.* **1975,** *13*, 142-59.
43. Bultinck, P.; Van Alsenoy, C.; Ayers, P. W.; Carbo-Dorca, R., *J. Chem. Phys.* **2007,** *126*, 144111.
44. Bultinck, P.; Ayers, P. W.; Fias, S.; Tiels, K.; Van Alsenoy, C., *Chem. Phys. Lett.* **2007,** *444*, 205-208.
45. Gaigalas, G.; Froese Fischer, C., *Comput. Phys. Commun.* **1996,** *98*, 255-264.
46. Otero-de-la-Roza, A.; Blanco, M. A.; Pendas, A. M.; Luana, V., *Comput. Phys. Commun.* **2009,** *180*, 157-166.
47. Otero-de-la-Roza, A.; Johnson, E. R.; Luana, V., *Comput. Phys. Commun.* **2014,** *185*, 1007-1018.
48. Halasyamani, P.; Willis, M. J.; Stern, C. L.; Lundquist, P. M.; Wong, G. K.; Poeppelmeier, K. R., *Inorg. Chem.* **1996,** *35*, 1367-71.
49. Thomas, P. M.; Norquist, A. J.; Doran, M. B.; O'Hare, D., *J. Mater. Chem.* **2003,** *13*, 88-92.
50. Nelson, J. H.; Johnston, A. R.; Narducci Sarjeant, A.; Norquist, A. J., *Solid State Sci.* **2007,** *9*, 472-484.
51. Harrison, W. T. A.; Dussack, L. L.; Jacobson, A. J., *J. Solid State Chem.* **1996,** *125*, 234-242.
52. Doran, M. B.; Norquist, A. J.; O'Hare, D., *Inorg. Chem.* **2003,** *42*, 6989-6995.

53. Bensch, W.; Hug, P.; Reller, A.; Oswald, H. R., *Mater. Res. Bull.* **1987,** *22*, 577-83.

54. Khan, M. I.; Hope, T.; Cevik, S.; Zheng, C.; Powell, D., *J. Cluster Sci.* **2000,** *11*, 433-447.

55. De Burgomaster, P.; Ouellette, W.; Liu, H.; O'Connor, C. J.; Yee, G. T.; Zubieta, J., *Inorg. Chim. Acta* **2010,** *363*, 1102-1113.

56. Roman, P.; Aranzabe, A.; Luque, A.; Gutierrez-Zorrilla, J. M., *Mater. Res. Bull.* **1991,** *26*, 19-27.

57. Tyrselova, J.; Pavelcik, F., *Acta Crystallogr., Sect. C Cryst. Struct. Commun.* **1992,** *C48*, 1207-9.

58. Duraisamy, T.; Ojha, N.; Ramanan, A.; Vittal, J. J., *Chem. Mater.* **1999,** *11*, 2339-2349.

59. Tyrselova, J.; Kuchta, L.; Pavelcik, F., *Acta Crystallogr., Sect. C Cryst. Struct. Commun.* **1996,** *C52*, 17-19.

60. Smith, M. D.; Blau, S. M.; Chang, K. B.; Tran, T. T.; Zeller, M.; Halasyamani, P. S.; Schrier, J.; Norquist, A. J., *J. Solid State Chem.* **2012,** *195*, 86-93.

61. Ferey, G., *Chem. Mater.* **2001,** *13*, 3084-3098.

62. Rao, C. N. R.; Natarajan, S.; Choudhury, A.; Neeraj, S.; Ayi, A. A., *Acc. Chem. Res.* **2001,** *34*, 80-87.

63. Rao, C. N. R.; Natarajan, S.; Neeraj, S., *J. Solid State Chem.* **2000,** *152*, 302-321.

64. Murugavel, R.; Walawalkar, M. G.; Dan, M.; Roesky, H. W.; Rao, C. N. R., *Acc. Chem. Res.* **2004,** *37*, 763-774.

65. Gautier, R.; Norquist, A. J.; Poeppelmeier, K. R., *Cryst. Growth Des.* **2012,** *12*, 6267-6271.

66. Veltman, T. R.; Stover, A. K.; Narducci Sarjeant, A.; Ok, K. M.; Halasyamani, P. S.; Norquist, A. J., *Inorg. Chem.* **2006,** *45*, 5529-5537.

67. Norquist, A. J.; Doran, M. B.; Thomas, P. M.; O'Hare, D., *Dalton Transactions* **2003**, 1168-1175.

68. Stover, A. K.; Gutnick, J. R.; Narducci Sarjeant, A.; Norquist, A. J., *Inorg. Chem.* **2007,** *46*, 4389-4391.

69. Koffer, J. H.; Olshansky, J. H.; Smith, M. D.; Hernandez, K. J.; Zeller, M.; Ferrence, G. M.; Schrier, J.; Norquist, A. J., *Cryst. Growth Des.* **2013,** *13*, 4504-4511.

70. Casalongue, H. S.; Choyke, S. J.; Narducci Sarjeant, A.; Schrier, J.; Norquist, A. J., *J. Solid State Chem.* **2009,** *182*, 1297-1303.

71. Chang, K. B.; Hubbard, D. J.; Zeller, M.; Schrier, J.; Norquist, A. J., *Inorg. Chem.* **2010,** *49*, 5167-5172.

72. Olshansky, J. H.; Blau, S. M.; Zeller, M.; Schrier, J.; Norquist, A. J., *Cryst. Growth Des.* **2011,** *11*, 3065-3071.

73. Chang, K. B.; Smith, M. D.; Blau, S. M.; Glor, E. C.; Zeller, M.; Schrier, J.; Norquist, A. J., *Cryst. Growth Des.* **2013,** *13*, 2190-2197.

74. Gutnick, J. R.; Muller, E. A.; Narducci Sarjeant, A.; Norquist, A. J., *Inorg. Chem.* **2004,** *43*, 6528-6530.

75. Muller, E. A.; Cannon, R. J.; Narducci Sarjeant, A.; Ok, K. M.; Halasyamani, P. S.; Norquist, A. J., *Cryst. Growth Des.* **2005,** *5*, 1913-1917.

76. Hubbard, D. J.; Johnston, A. R.; Sanchez Casalongue, H.; Narducci Sarjeant, A.; Norquist, A. J., *Inorg. Chem.* **2008,** *47*, 8518-8525.

77. Olshansky, J. H.; Thao Tran, T.; Hernandez, K. J.; Zeller, M.; Halasyamani, P. S.; Schrier, J.; Norquist, A. J., *Inorg. Chem.* **2012,** *51*, 11040-11048.

78. Johnson, E. R.; Keinan, S.; Mori-Sanchez, P.; Contreras-Garcia, J.; Cohen, A. J.; Yang, W., *J. Am. Chem. Soc.* **2010,** *132*, 6498-6506.

79. Otero-de-la-Roza, A.; Johnson, E. R.; Contreras-Garcia, J., *PCCP* **2012,** *14*, 12165-12172.
80. Yang, J.; Waller, M. P., *J. Comput. Chem.* **2013,** *34*, 466-470.
81. Paliwal, S.; Geib, S.; Wilcox, C. S., *J. Am. Chem. Soc.* **1994,** *116*, 4497-4498.